Chinese Journal of Chemical Engineering 95 (2026) 347–360

Contents lists available at ScienceDirect

Chinese Journal of Chemical Engineering

journal homepage: www.elsevier.com/locate/CJChE

Full Length Article

Investigating flow field control mechanisms in a molten bath using POD and chaos theory with asymmetric nozzle arrangements

Yu Wang [1, 2, 3], Tong Meng [2, 3], Shuang Qin [2, 3], Guocan Zheng [1, 2, 4], Jun Du [2, 3], Shibo Wang [1, 5], Changyuan Tao [2, 3], Zuohua Liu [2, 3, *]

[1] State Key Laboratory of Complex Nonferrous Metal Resources Clean Utilization, Kunming University of Science and Technology, Kunming 650093, China
[2] School of Chemistry and Chemical Engineering, Chongqing University, Chongqing 400044, China
[3] State Key Laboratory of Coal Mine Disaster Dynamics and Control, Chongqing 400044, China
[4] Analytical and Testing Center, Chongqing University, Chongqing 400044, China
[5] Faculty of Metallurgical and Energy Engineering, Kunming University of Science and Technology, Kunming 650093, China

ARTICLE INFO

Article history:
Received 24 October 2025
Received in revised form
21 February 2026
Accepted 25 February 2026
Available online 20 April 2026

Keywords:
Proper orthogonal decomposition (POD)
Chaos theory
Bottom-blown stirring
Asymmetric nozzle arrangement
Energy cascade

ABSTRACT

The flow regulation mechanism of bottom-blowing stirring is the key to enhancing the reaction efficiency of a molten bath. Herein, proper orthogonal decomposition (POD) is integrated with chaos theory for the first time to investigate the influence of asymmetric nozzle arrangements on flow field regulation and mixing performance during bottom-blowing smelting. The optimization effect of a 10° asymmetric nozzle configuration (model III) is specifically examined through numerical simulation and analysis. The results indicate that model III effectively suppresses splashing while increasing splash height and optimizing the flow field structure, thereby markedly enhancing mixing efficiency. The Lyapunov exponent in the main flow region is 1.5–2.3 times higher than that of other models, and energy cascades across the full frequency range of 50–300 Hz. POD analysis reveals that approximately 98% of the total system energy is captured by the first 68 modes, while the first two modes together account for 71.36% of the total energy, indicating a highly efficient low-order energy representation and rapid energy transfer across dominant flow structures. The asymmetric vortex structure effectively coordinates large macroscopic vortices and small-scale eddies, thereby enhancing mixing performance. This work provides theoretical support for the optimization of bottom-blowing furnace stirring systems and demonstrates the potential of POD in metallurgical process analysis.
© 2026 The Chemical Industry and Engineering Society of China, and Chemical Industry Press Co., Ltd. All rights are reserved, including those for text and data mining, AI training, and similar technologies.

1. Introduction

In the field of copper metallurgy, bottom-blowing smelting technology has been established as a core process in modern copper production owing to its high-efficiency mixing and environmentally benign characteristics [1–5]. The arrangement strategy of a nozzle array, as a key system component, directly determines gas jet behavior and bath circulation patterns, thereby causing multidimensional effects on reaction efficiency, energy consumption, and furnace service life [6–8]. However, the chaotic motion mechanisms of multiphase fluids within the bath remain a central challenge in achieving precise process optimization.

To address this challenge, extensive study has been conducted on the parametric design of nozzles, primarily focusing on spatial arrangement, quantity configuration, and geometric parameters. Previous studies have largely focused on symmetrical arrangements, which produce an unfavorable flow state, in which high-speed shear zones coexist with flow dead zones, thereby limiting further improvements in mixing efficiency [9–12]. Although asymmetric configurations have been demonstrated to enhance gas–liquid contact and expand high-velocity flow regions [13–15], they are accompanied by sidewall erosion caused by melt convergence and nonlinear surface oscillations, resulting in a pronounced trade-off between efficiency gains and equipment durability. In terms of quantity configuration, the number of nozzles has been shown to exhibit a nonlinear relationship with mixing efficiency. Beyond a critical value, mixing time is no longer markedly reduced by flow field interference effects [16,17]. As a key geometric parameter, nozzle diameter influences bubble

* Corresponding author.
E-mail address: liuzuohua@cqu.edu.cn (Z. Liu).

https://doi.org/10.1016/j.cjche.2026.02.014
1004-9541/© 2026 The Chemical Industry and Engineering Society of China, and Chemical Industry Press Co., Ltd. All rights are reserved, including those for text and data mining, AI training, and similar technologies.

dynamics by regulating gas flux. An increase in diameter not only enhances melt turbulence but also promotes bubble coalescence and splashing [18,19]. The effect of gas flow rate on mixing behavior leads to nonlinear characteristics: the mixing efficiency initially increases and then decreases with increasing flow rate, deteriorating beyond an optimum level owing to channeling effects [20,21]. However, most of these studies focus on macroscopic mixing performance, while a systematic and in-depth investigation of the complex fluid dynamic behavior in a stirred bath, particularly the chaotic flow characteristics induced by asymmetric nozzles and their correlation with mixing efficiency, is still lacking. Bottom-blowing stirring is inherently a highly turbulent process; in this process, complex vortex structures and multiscale flow phenomena directly govern interphase transport and ultimately affect metallurgical homogeneity. Therefore, accurately describing and understanding the flow characteristics and turbulent structures across different scales are considered key to overcoming current research bottlenecks.

Advances in computational fluid dynamics (CFD) have essentially supported the addressal of the abovementioned challenges [22,23]. CFD has macroscopically verified the advantages of asymmetric nozzle configurations in mixing efficiency [24–26] and enabled accurate prediction of bubble dynamics, such as coalescence and breakup, at a micro-mechanistic level, while also revealing the formation conditions and nonlinear evolution of surface standing waves [27–29]. However, advanced flow field identification methods are required to deeply analyze the complex flow structures and multiscale turbulence features revealed by CFD. Proper orthogonal decomposition (POD), a powerful reduced-order modeling and modal analysis technique, has been widely applied in turbulence and multiphase flow research [30,31]. Its core advantage lies in its ability to extract dominant low-dimensional coherent structures from high-dimensional transient flow fields and to quantify the contribution of vortex structures at different scales to turbulent energy *via* modal energy distribution [32–34]. In the field of stirring, POD has been successfully employed to identify coherent structures in reactors and to reveal vortex shedding and periodic fluctuations induced by impellers [35]. Our previous work demonstrates that POD can effectively resolve the coupling mechanism of multiscale vortex structures in flow fields [36,37], highlighting its potential for revealing the nature of complex flows and providing key insights into the optimization of molten pool stirring processes.

Nevertheless, studies on the application of POD in the chaotic flow systems induced by asymmetric nozzles are limited. Such flows are characterized by strong nonlinearity and multimodal coupling. Conventional POD analysis is often restricted to modal energy ranking and has not been completely integrated with dynamical systems theory to reveal the intrinsic relationship between modal evolution and mixing efficiency. Chaotic dynamics theory is an effective tool for quantifying the nonlinear evolution behavior of such systems. Indices such as the largest Lyapunov exponent (LLE) can quantitatively characterize the sensitivity of a system to initial conditions and describe the nonlinearity and instability of flow from a dynamic perspective [38–40]. Chaotic behavior has been shown to be a crucial dynamic characteristic of turbulence. Its intensification often means rapid separation of fluid particle trajectories and more complete cross-scale interactions, which is conducive to the advancement of mixing process. The phase dynamics of the POD time coefficient can reflect the energy transfer law between multiscale structures [41]. Therefore, the integration of POD with chaos theory is expected to systematically reveal the flow field regulation mechanism under asymmetric nozzle arrangements, thereby addressing a research gap in this area. On this basis, herein, asymmetric dual-row nozzles are considered the research object. POD analysis is innovatively integrated with chaos theory, and the flow characteristics are analyzed from both structural and dynamical perspectives, providing a new theoretical basis for process optimization and equipment design.

Unlike conventional analyses based on velocity fields, turbulent kinetic energy, or global mixing indices, this work employs POD- and chaos theory-based analysis to reveal the intrinsic mechanisms of mixing enhancement induced by asymmetric nozzle configurations from a modal-dynamics perspective. POD quantitatively describes the spatial organization and energy distribution of multiscale vortex structures, while chaos analysis characterizes the nonlinear intensity and instability of flow evolution using time-series information. Unlike a simple superposition of the two methods, their combined use enables mutual verification between modal structural features and chaotic intensity, thereby establishing a physical linkage between the enhancement of flow nonlinearity, the activation of cross-scale energy transfer, and the improvement of mixing efficiency in asymmetric nozzle systems. This approach transcends traditional frameworks that rely solely on macroscopic flow characteristics or single statistical indicators.

Following the abovementioned research approach, the POD method and chaos theory are integrated to systematically investigate the influence of different nozzle arrangements on the multiscale flow field structure and evolutionary dynamics in a bottom-blown molten pool. Under the same gas flow conditions, five nozzle configurations, such as a single nozzle at 0°, dual nozzles at 10° symmetric, dual nozzles at 10° asymmetric, dual nozzles at 20° symmetric, and dual nozzles at 20° asymmetric, are compared to build a multidimensional analysis framework. First, the macroscopic mixing advantage of the asymmetric arrangement is verified on the basis of bubble dynamics. Subsequently, the Lyapunov exponent is used to quantify the chaotic intensity of the system. Evidently, the small-angle asymmetric model (model III) exhibits the most important chaotic characteristics. Furthermore, synchronous continuous wavelet transform is applied to analyze the time–frequency coordination characteristics of multiscale vortex structures. Emphasis is placed on integrating POD analysis throughout the flow field structure analysis: dominant vortex structures are identified through modal energy distribution and the enhancement mechanism of asymmetric vortex pairs on the energy cascade is revealed by combining streamline topology. By comparing the dynamic evolution of high-order modal time coefficients, the modulation effect of asymmetric nozzles on the spatiotemporal redistribution of turbulent energy is elucidated from the perspective of POD modal dynamics. For the first time, this work deeply integrated chaos theory and POD in the field of molten pool stirring, revealing the essential mechanism by which asymmetric nozzles enhance mixing *via* multiscale vortex coordination from a flow field dynamics perspective.

2. Geometric Model and Analysis Methods

2.1. Geometric model

This work focuses on a large Φ4.4 m × 30 m oxygen bottom-blown furnace in a copper smelter and analyzes the configuration characteristics of its core component, the oxygen lance system, and its mechanism of influence on the molten metal flow behavior. Previous studies on bottom-blown metallurgical furnaces and gas stirring systems have shown that small-angle asymmetric nozzle disturbances can considerably affect the primary circulation structure and vortex morphology of a molten pool, while excessively large nozzle offset angles often result in unfavorable engineering consequences, such as molten metal

deflection, increased splashing, and intensified sidewall erosion [18,19]. Based on this understanding, this work compares the flow characteristics under two layouts: staggered oxygen lances and a single oxygen lance. Five model schemes are constructed, including a single oxygen lance layout and symmetric and asymmetric nozzles with inclination angles of 10°–20°. The specific angle and layout are shown in Fig. 1.

This work deeply investigates the role of pneumatic stirring in the furnace body by focusing on the angle and layout of the oxygen gun: Model I constitutes the control group, a single oxygen gun layout. Models II and III correspond to the center cross-section of the furnace diameter of the 10° angle oxygen gun group, focusing on the analysis of the melt pool dynamics under the action of oxygen guns with a small inclination angle. Models IV and V correspond to the center section of the furnace diameter of the 20° angle oxygen lance group, focusing on the aerodynamic stirring characteristics of the oxygen lance with a large inclination angle. Each model features five monitoring points (P1–P5) near the gas–slag and matte–slag interfaces to monitor flow field parameters in real time. The interface region of the bottom-blown molten pool exhibits the strongest flow nonlinearity and pulsation and is highly sensitive to the changes in nozzle angle. Therefore, it can effectively characterize the flow field dynamics under different operating conditions. The interface position is kept consistent across all models to ensure comparability of the monitoring signals. This work reveals the influence of oxygen lance angle differences on mixing efficiency by comparing and analyzing the flow field parameters under different configurations.

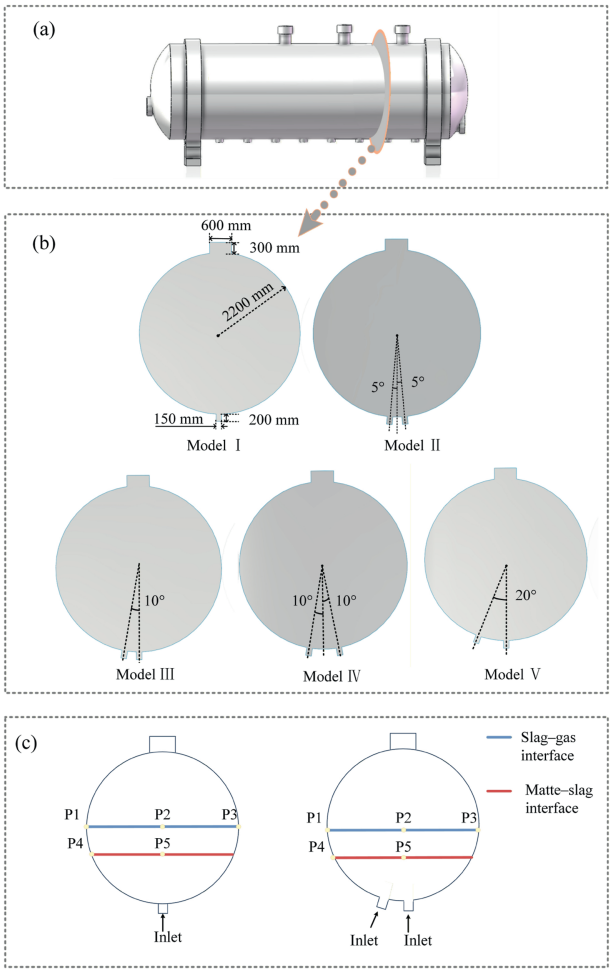


Fig. 1. Large-scale bottom-blown furnace model: (a) three-dimensional (3D) prototype of the equipment; (b) two-dimensional (2D) structural schematics; (c) schematics of phase interface monitoring line distribution.

2.2. Definition of metrics

2.2.1. Largest Lyapunov exponents

While calculating, pressure fluctuation is monitored at five locations, as shown in Fig. 1(c), with a sampling frequency of 10000 Hz. The LLE is a crucial invariant for detecting and characterizing chaos in dynamical systems, quantifying the average exponential rate of convergence or divergence between adjacent trajectories in phase space [42].

Herein, the Lyapunov exponent is calculated directly using the raw pressure fluctuation signals obtained from the CFD monitoring points. Since the numerical signals are free from measurement noise, no additional filtering or smoothing is applied before phase–space reconstruction. First, a phase–space reconstruction strategy based on the C–C method is used to determine the time delay parameter τ and the embedding dimension m is determined by combining it with the spurious nearest neighbor criterion. A reference trajectory initial point $X(t_0)$ is selected, and its nearest neighbor point $X(t_k)$ (minimizing Euclidean distance) is identified in the phase space. The evolutionary directions of both the trajectories are continuously tracked until their separation distance $d(t) = \|X(t_i) - X(t_j)\|$ first exceeds a preset threshold ε, at which point the tracking is terminated and the evolution duration Δt is recorded. Subsequently, valid neighboring points that satisfy $\|X(t_i + \Delta t) - X(t_j)\| < \varepsilon/3$ are reselected at the specified time. A local linear approximation of divergence paths is constructed through iterative optimization (total iterations M). Finally, on the basis of exponential divergence characteristics, the LLE is calculated using the following equation:

$$\mathrm{LLE} = \lim_{\Delta t \to \infty} \frac{1}{M \Delta t} \sum_{k=1}^{M} \ln \frac{d_k(t + \Delta t)}{d_k(t)} \tag{1}$$

where $d_k(t)$ represents the initial spacing during the kth iteration and $d_k(t+\Delta t)$ denotes the diverged spacing. This algorithm employs local linearization to process nonlinear trajectory evolution, effectively characterizing the sensitivity of the system to initial conditions.

2.2.2. Synchrosqueezed wavelet transform (SWT)

This work employs the SWT for time–frequency analysis of pressure fluctuation signals to deeply analyze the spatiotemporal evolution characteristics of multiscale vortex structures in the flow field of a structured stirred reactor. Compared with conventional wavelet transforms, SWT notably enhances time–frequency resolution by compressing wavelet coefficients toward instantaneous frequency curves, making it particularly suitable for refined decomposition of nonstationary turbulent signals [43]. The SWT method, which is based on the Morlet wavelet, defines its core wavelet function as:

$$\psi(t) = \pi^{(-1/4)} \mathrm{e}^{(i\omega t)} \mathrm{e}^{(-t^2/2)} \tag{2}$$

where t denotes time, i is the imaginary unit, and ω denotes the central frequency of the Morlet wavelet. The wavelet combines temporal localization and spectral smoothness, enabling effective capture of signal fluctuations induced by vortices across scales—from large-scale low-frequency vortices to small-scale high-frequency vortices.

2.2.3. Proper orthogonal decomposition

The flow field ubiquitously exhibits coherent structures that integrate regularity and stochasticity, with such multiscale vortex systems playing a central regulatory role in heat and mass transfer processes. To quantitatively resolve these dynamical features, Lumley [44] pioneered the introduction of POD into fluid mechanics, a method that achieves energy-optimal characterization of turbulent coherent structures through eigenmode extraction. In subsequent developments, building on the snapshot POD algorithm proposed by Sirovich [45], researchers gained the capability to efficiently process high-dimensional flow field data. Fukunaga [46] further demonstrated the linear positive correlation between modal eigenvalues and velocity fluctuation energy distribution, providing mathematical validation for cross-scale energy distribution mechanisms of turbulent kinetic energy. POD is currently established as a core analytical tool in turbulence research.

3. Computational Model and Numerical Methods

3.1. Hydrodynamic model

Herein, a two-dimensional (2D) pneumatic stirring numerical model of a large bottom-blowing melting furnace is constructed on the basis of the conservation equation. The standard k–ε turbulence model and the volume of fluid (VOF) multiphase flow model are used for coupling calculation. Considering the complexity of multiphase multifield coupling in copper smelting, the following simplification strategies are implemented in the modeling process: (1) the steady-state simulation excludes the transient interference of the charging/discharging operation; (2) the reaction system is simplified as a physical flow process, and the thermal effect of the chemical reaction is ignored; and (3) the assumption of independent oxygen lances is adopted in the 2D modeling, and the influence of the interaction between oxygen lances is not considered.

3.1.1. Governing equations

In the large bottom-blowing furnace pneumatic stirring process, mass, momentum, and heat transfer occur between the bottom-blowing gas and the material phase. The basic control equations governing the entire process are as follows.

Mass conservation equations:

$$\frac{\partial \rho}{\partial t}+\frac{\partial(\rho u_i)}{\partial x_i}=0 \tag{3}$$

Momentum conservation equation:

$$\frac{\partial(\rho u_i)}{\partial t}+\frac{\partial\left(\rho u_i u_j\right)}{\partial x_j}=-\frac{\partial p}{\partial x_i}+\frac{\partial \tau_{ij}}{\partial x_j}+\rho g_i+f_\sigma \tag{4}$$

The energy conservation equation:

$$\frac{\partial\left(\rho C_p T\right)}{\partial t}+\frac{\partial\left(\rho u_j C_p T\right)}{\partial x_i}=u\frac{\partial p}{\partial x_i}+\tau_{ij}\frac{\partial u_i}{\lambda_{\text{eff}}}+\lambda_{\text{eff}}\frac{\partial^2 T}{\partial x_i^2} \tag{5}$$

where fluid density is ρ ($\mathrm{kg\cdot m^{-3}}$); u_i and u_j ($\mathrm{m\cdot s^{-1}}$) represent the velocity components in the i and j directions, respectively; p (Pa) denotes the static pressure; and g_i ($\mathrm{m\cdot s^{-2}}$) corresponds to the spatial component of the gravitational acceleration. The external volumetric force source term σ ($\mathrm{N\cdot m^{-3}}$) characterizes the intensity of the external force action; C_p ($\mathrm{J\cdot kg^{-1}\cdot K^{-1}}$) refers to the specific heat capacity; and T (K) denotes the temperature. Dynamic viscosity μ (Pa·s) is associated with the viscous stress tensor component τ_{ij} (Pa), and λ_{eff} ($\mathrm{W\cdot m^{-1}\cdot K^{-1}}$) denotes effective thermal conductivity.

3.1.2. VOF phase equations

The three-phase coupled motion characteristics of the gas–slag layer–matte phase system in copper smelting exhibit distinct free interface features, with the interface morphology changing drastically over time. The VOF model is considerably advantages in tracking interfaces in multiphase fluid flow [25,47]. Therefore, herein, the VOF model in Fluent is used for interface trapping. The VOF model introduces a volume fraction α to simulate the flow of multiple immiscible fluids by solving a set of momentum equations and tracking the volume fraction α of each fluid in the whole region. The model volume fraction equations are as follows [48]:

$$\frac{\partial \alpha_q}{\partial t}+\nabla\cdot\left(\alpha_q \boldsymbol{u}\right)=0 \tag{6}$$

$$\sum_{q=1}^{n}\alpha_q=1 \tag{7}$$

where α_q denotes the volume fraction of the qth phase. $\alpha_q=1$ indicates that the volume cell has all q phases, $\alpha_q=0$ indicates that the volume cell has no q phases, and $0<\alpha_q<1$ indicates that the volume cell has q phases as well as other phases.

The equivalent physical properties of multiphase systems are obtained by weighting according to the volume fraction, and their mixture density and dynamic viscosity are expressed as follows [48]:

$$\rho=\sum_{q=1}^{n}\alpha_q\rho_q \tag{8}$$

$$\mu=\sum_{q=1}^{n}\alpha_q\mu_q \tag{9}$$

The interface morphology exhibits highly unsteady evolutionary characteristics over time owing to the considerable density difference between the gas and liquid phases in the bottom-blown molten pool and the intense processes of bubble generation, rising, merging, and free surface fluctuation. On the basis of these flow characteristics, this work uses the VOF method to describe the gas–slag–matte multiphase interface. Within the VOF framework, the density and viscosity of the multiphase system are updated using a volume fraction weighting method and a geometric reconstruction scheme is employed for interface capturing, thereby improving the numerical stability and accuracy of interface tracking under high-density ratio conditions. This method excellently balances the interface capturing accuracy and computational efficiency, with the ability to accurately reflect the transient evolution process of the gas–slag–matte multiphase interface, providing a reliable numerical basis for subsequent POD analysis and the investigation of chaotic characteristics based on transient flow field data.

3.1.3. Turbulence model equations

Considering the violent reaction in the large smelting bottom-blowing melt pool, the standard k–ε model, which is widely applicable, is selected as the turbulence model to simulate the large copper smelting bottom-blowing melt pool. The corresponding model control equations are expressed in Eqs. (10) and (11).

Turbulent kinetic energy k equation:

$$\frac{\partial(\rho k)}{\partial t}+\frac{\partial(\rho k u_i)}{\partial x_i}=\frac{\partial}{\partial x_j}\left[\left(\mu+\frac{\mu_t}{\alpha_k}\right)\frac{\partial k}{\partial x_j}\right]+G_k+G_b-\rho\varepsilon-Y_M+S_k \tag{10}$$

Dissipation rate ε equation:

$$\frac{\partial(\rho\varepsilon)}{\partial t}+\frac{\partial\left(\rho\varepsilon u_j\right)}{\partial x_j}=\frac{\partial}{\partial x_j}\left[\left(\mu+\frac{\mu_t}{\alpha_\varepsilon}\right)\frac{\partial\varepsilon}{\partial x_j}\right]+\rho C_1 S_\varepsilon-\rho C_2\frac{\varepsilon^2}{k+\sqrt{\nu\varepsilon}}+C_{1\varepsilon}\frac{\varepsilon}{k}C_{3\varepsilon}G_b+S_\varepsilon \tag{11}$$

where

$$C_1=\max\left[0.43,\frac{\eta}{\eta+5}\right] \tag{12}$$

$$\eta=S\frac{k}{\varepsilon} \tag{13}$$

$$S=\sqrt{2}S_{ij} \tag{14}$$

$$S_{ij}=\frac{1}{2}\left(\frac{\partial u_i}{\partial x_i}+\frac{\partial u_j}{\partial x_j}\right) \tag{15}$$

where G_k ($kg\cdot m^{-1}\cdot s^{-3}$) denotes the turbulent kinetic energy generated by the mean velocity gradient; G_b ($kg\cdot m^{-1}\cdot s^{-3}$) denotes the turbulent kinetic energy generated by the effect of buoyancy; Y_M ($kg\cdot m^{-1}\cdot s^{-3}$) denotes the effect of pulsating expansion of compressible turbulence on the total dissipation rate; μ (Pa·s) denotes the dynamic viscosity; μ_t (Pa·s) denotes the turbulent viscosity; ε ($m^2\cdot s^{-3}$) denotes the turbulent dissipation rate; k ($m^2\cdot s^{-2}$) denotes the turbulent kinetic energy; S (s^{-1}) denotes the mean strain rate; C_1 and η are coefficients; S_{ij} denotes the strain rate tensor; α_k is the Prandtl number corresponding to the turbulent kinetic energy k; α_ε is the Prandtl number corresponding to the dissipation rate ε; S_k and S_ε are user-defined source terms; $C_{1\varepsilon}$, C_2, and $C_{3\varepsilon}$ are empirical constants. $C_{3\varepsilon}$ is a buoyancy-related coefficient and is modeled as a function of the flow and gravity directions; therefore, its value depends on the buoyancy configuration. The standard k–ε turbulence model parameters take the following values: $C_{1\varepsilon}$= 1.44, C_2 = 1.92, α_k= 1.0, and α_ε= 1.3.

3.2. Boundary conditions and physical parameters

As smelting in large bottom-blowing furnaces requires attention to the gas–matte–slag interaction in the molten pool, transient calculations are used. The velocity–pressure coupling is realized with the help of the PISO algorithm, and the pressure term in the velocity-correction equation is discretized using the PRESTO scheme. The volume fraction equation is geometrically reconstructed; the momentum, turbulent kinetic energy, turbulent dissipation rate, and energy are calculated using the second-order windward format to ensure the accuracy of the calculation.

A velocity inlet boundary condition is used for gas inlet. For the dual-inlet nozzle configuration, the gas velocity at each inlet is set to 10 $m\cdot s^{-1}$; for the single-inlet nozzle configuration, the inlet velocity is correspondingly set to 20 $m\cdot s^{-1}$ to ensure that the total gas input remained constant within the dual-inlet configuration. This equivalent gas input method ensures that different models maintain consistent overall gas flow rate and momentum input levels, thus guaranteeing the fairness and interpretability of the flow field comparison analysis under different nozzle arrangements.

Table 1
Physical parameters of the three phases in a large bottom-blowing furnace.

Parameters	Air phase	Copper slag phase	Copper sulfonium phase
Density/$kg\cdot m^{-3}$	Ideal gas	3500	5000
Viscosity/Pa·s	1.79×10^{-5}	0.15	0.03
Specific heat capacity/$J\cdot kg^{-1}\cdot K^{-1}$	1066.43	1260	600
Initial temperature/K	298.15	1503.15	1473.15
Thermal conductivity/$W\cdot m^{-1}\cdot K^{-1}$	0.024	1.2	3

Initialization is performed using the standard initialization method, and the inlet is used as the starting position to complete the initialization of the computational domain. The melt region is initialized locally using the Patch function. The time step is set at 0.001 s, and the number of time steps for the solution is 10000, with 10 s for the transient solution.

The position of the oxygen gun of the large bottom-blowing furnace is set as the mass flow inlet, where the inlet medium is air, and the inlet mass flow rate is calculated to be 0.67 $kg\cdot s^{-1}$ according to the actual working conditions (the speed is set at 13 $m\cdot s^{-1}$). The velocities of the dual nozzles are 9 and 4 $m\cdot s^{-1}$, respectively, and all models are evaluated under the same gas flow rate. The flue gas outlet at the top of the large bottom-blowing furnace is set as the pressure outlet, and the outlet exhibits a slightly negative pressure (−20 Pa). The wall surface is set as a standard wall function. The fluid in the large bottom-blowing furnace is divided into three phases, namely, air phase, copper matte phase, and copper slag phase, and the physical parameters of each phase are listed in Table 1.

3.3. Grid independence verification

Herein, a nonstructural mesh is used, with the global mesh size of models I–V is set to 20 mm. A workbench-meshing software is used to perform mesh delineation. After the mesh is generated (Fig. 2), the average values of the mesh quality indexes reaches above 0.9, the skewness indexes all below 0.95, the mesh quality remains within the acceptable range, and the next step of the computation can be conducted.

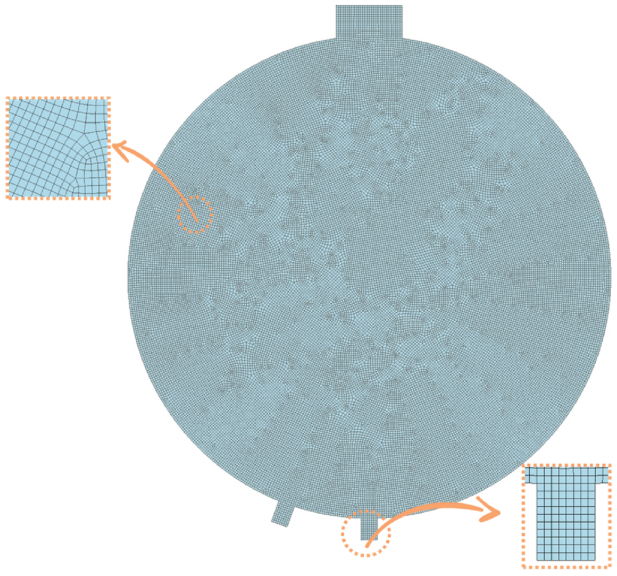


Fig. 2. Schematic of the grid division.

To verify the grid independence of the numerical calculation results, model I is selected as a representative case. Considering that the models only differ in nozzle structural parameters, while the remaining geometric configurations and operating conditions remain consistent, the flow characteristics are highly comparable. Therefore, grid independence verification is not repeated for the other models. For model I, three computational grids with mesh sizes of 18, 20, and 22 mm are constructed. The radial fluid velocity distribution at a cross-section near the inlet (y= 400 mm) is compared for different mesh sizes, where the radial coordinate x is normalized by the molten bath diameter D. As shown in Fig. 3, the overall velocity distribution exhibits a consistent trend across different mesh sizes. Using the 20 mm mesh as a reference, the deviations from the results obtained with the 18 and 22 mm meshes are 18.97% and 14.84%, respectively, with no systematic bias. This indicates that within the current range of mesh sizes, the calculation results exhibit good stability with respect to mesh scale. Owing to a comprehensive trade-off between accuracy and computational cost, a computational grid with a mesh size of 20 mm is consistently used in subsequent numerical simulations.

3.4. Model validity verification

First, the control equation system, VOF multiphase flow interface capturing method, and standard k–ε turbulence model are all widely used and well-established modeling combinations that have been extensively studied and validated in the context of bottom-blown metallurgical furnaces and gas–stirred metallurgical systems. The VOF method can dynamically track the gas–liquid (or gas–slag–matte) free interface through volume fraction transport, making it suitable for problems with strong interface deformation, such as bubble plumes and free surface fluctuations. The standard k–ε model can represent the dominant turbulent characteristics in bottom-blown stirring flow at the engineering scale with high computational efficiency. These methods have been widely used in CFD studies of SKS bottom-blown copper smelting furnaces, asymmetric bottom-blown conditions, and gas–stirred ladles/molten pools; they have achieved reasonable flow and mixing prediction results [49–52]. The numerical implementation and solution settings of the relevant models refer to the methods recommended in the Fluent theory guide [48], thus providing a reliable transient flow field data basis for the subsequent POD and chaotic characteristics analysis in this work.

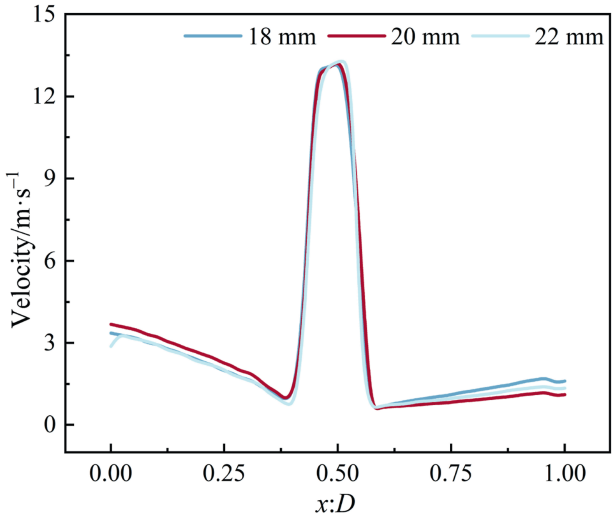


Fig. 3. Radial velocity distributions at different mesh sizes.

4. Results and Discussion

4.1. Bubble dynamic behavior

Bubble dynamics, a core physical process that determines the efficiency of smelting, directly govern the flow field structure and mixing performance through bubble deformation and movement patterns. Fig. 4 clearly reveals the intrinsic relationship between bubble dynamic behavior and macroscopic process parameters by systematically comparing the bubble rise and deformation processes under different models. According to temporal evolution, this process can be divided into three distinct stages.

In the initial stage (t= 0.3–0.6 s, corresponding to Fig. 4(a) and (b)), the bubble generation and initial interaction characteristics of each model show considerable differences. Notably, in model I, the bubbles, although highly spherical, are overly dispersed and fail to effectively aggregate owing to the excessively high jet velocity. In model II, the bubbles are too small and the distance between them is inappropriate, resulting in low coalescence efficiency and hindering further development. By contrast, model III, with optimized air inlet spacing, shows effective bubble edge coalescence at this stage, laying the dynamic foundation for the formation of dominant large bubble clusters. Remarkably, in models IV and V, the bubbles grow independently without any coalescence observed owing to the excessively large inlet spacing.

As the process progresses to the middle stage (t= 0.9 s), the differences in bubble morphology and flow field driving capability become more pronounced. In model I, the bubbles evolve into a cap-like shape and their straight-line ascent trajectory indicates substantial impact energy and potential splashing risks. In model II, the merged bubbles exhibit a considerable volume, maintain high sphericity, and have stable trajectories. Nevertheless, their regular shape and steady ascent path result in low energy transfer efficiency, failing to effectively convert buoyancy into large-scale molten bath convection. At this stage, the advantages of model III become clear. It forms a structure with a large dominant bubble core surrounded by a bubble group of different size ranges. Its buoyancy output markedly outperforms the other models, thereby effectively driving the molten bath to form strong convection. Conversely, the independently growing bubbles in models IV and V cause interference between the flow fields, leading to overall instability.

In the later stable stage (t= 2.0 s), the final performance and drawbacks of each model become evident. The flow field in model I exhibits excessive splashing, causing considerable energy dissipation owing to surface dispersion and furnace wall impacts. This results in a low energy efficiency ratio and a high risk of equipment wear. In model II, clear boundaries of unmixed regions remain visible, demonstrating that its energy is primarily dissipated in local splashing rather than effective global mixing. Remarkably, in model III, the splashing height is kept at a moderate level through precise control; this minimizes the equipment impact while completely activating the mixing space of the molten pool. It establishes a stable “rise–fall–rise” periodic circulation flow pattern, achieving efficient internal energy circulation. In comparison, although models IV and V exhibit the lowest splashing height, which is more equipment-friendly, their flow field lacks sufficient kinetic energy, which leads to underutilization of the mixing space and limits mixing efficiency.

Overall analysis shows that model III, through precise control of jet velocity and bubble coalescence dynamics, successfully balances buoyancy strength and flow field stability, thereby demonstrating comprehensive advantages in mixing efficiency, energy optimization, and equipment protection. The results of bubble dynamics clearly confirm the inherent advantages of asymmetric

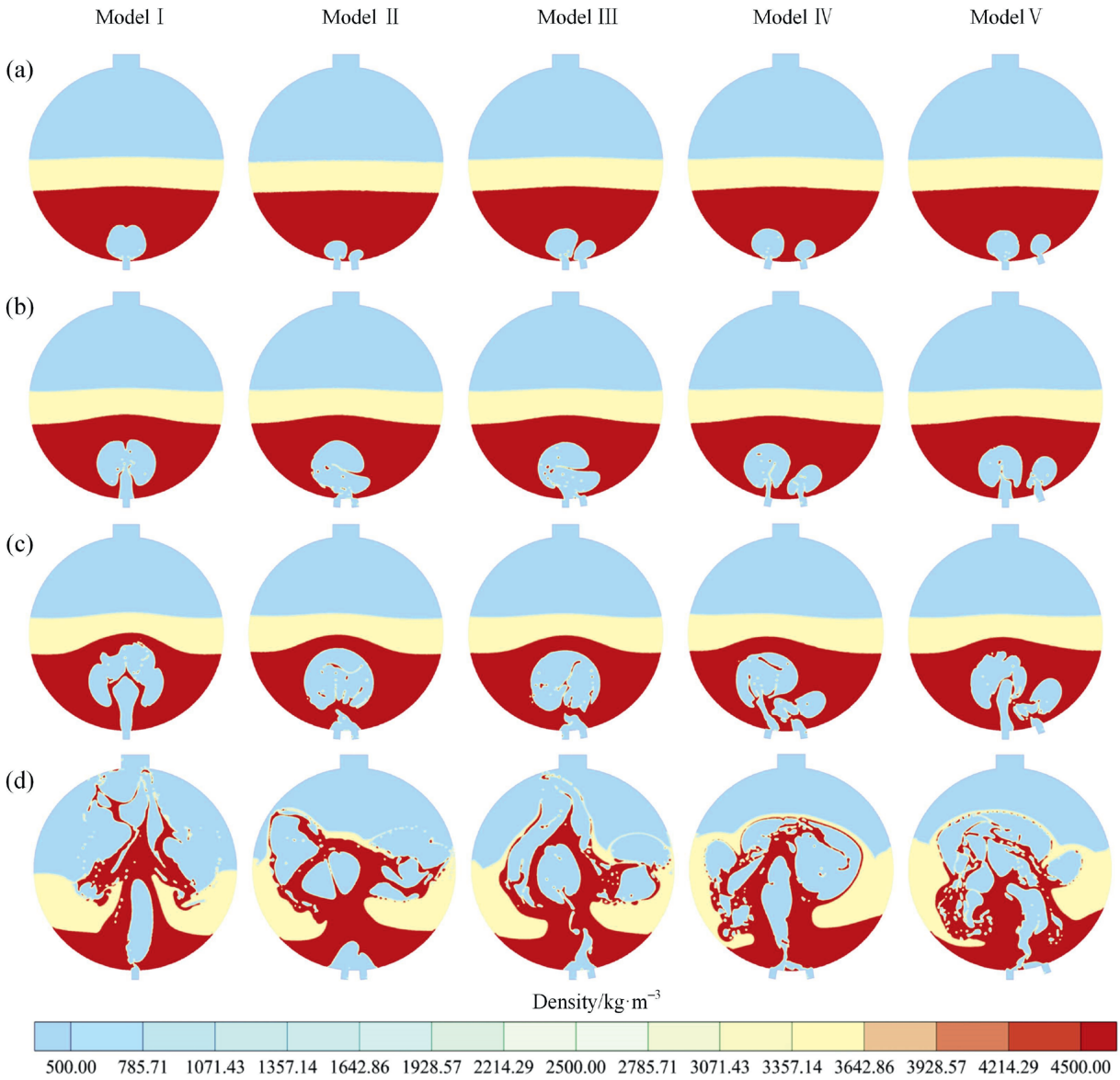


Fig. 4. Bubble ascent and deformation processes under different models: (a) 0.3 s, (b) 0.6 s, (c) 0.9 s, and (d) 2 s.

bubble structures in optimizing the flow field. However, the deeper mechanisms and quantitative relationships of the way this asymmetric structure induces and enhances chaotic mixing remain a key scientific issue that warrants further exploration.

4.2. Largest Lyapunov exponents

Pressure fluctuations, as a direct manifestation of energy transport and gas–liquid interactions within the molten bath, reflect the intrinsic dynamic characteristics of the system through their signal features. Therefore, analyzing the pressure fluctuation distribution at three key monitoring positions, P1, P4, and P5, is of particular importance. Notably, the time-domain analysis of the pressure fluctuation signals in Fig. 5 shows that all five models exhibit typical nonperiodic oscillation characteristics. However, model III remarkably demonstrates the most intense fluctuation behavior. Its signal contains both large-scale low-frequency undulations and high-frequency abrupt changes, strongly indicating the presence of more complex chaotic dynamics within the system. To further explore this intriguing phenomenon and quantitatively characterize it, this work employs the LLE to analyze the pressure fluctuation signals at the main flow regions, P1–P5, for all five models.

Fig. 6 shows the LLE calculated from the pressure fluctuation signals at five monitoring positions in the main flow region for all five models to quantitatively assess the turbulent mixing characteristics of each model. Notably, the lines connecting the LLE values at different monitoring points in Fig. 6 are only used to visually compare the differences in the chaotic intensity of the different models at different locations and not for representing their continuous spatial distribution trend. The analysis reveals that the LLE values for models I, II, and IV are greater than zero, indicating that the systems are sensitive to initial conditions. However, their values are generally low, which reflects their weak chaotic intensity in flow fields. Remarkably, the LLE for model III remains markedly higher at all positions than that of the other models. In particular, at P2 (0.56) and P4 (0.68), the LLE reaches peaks that are 1.5–2.3 times stronger than those of the other

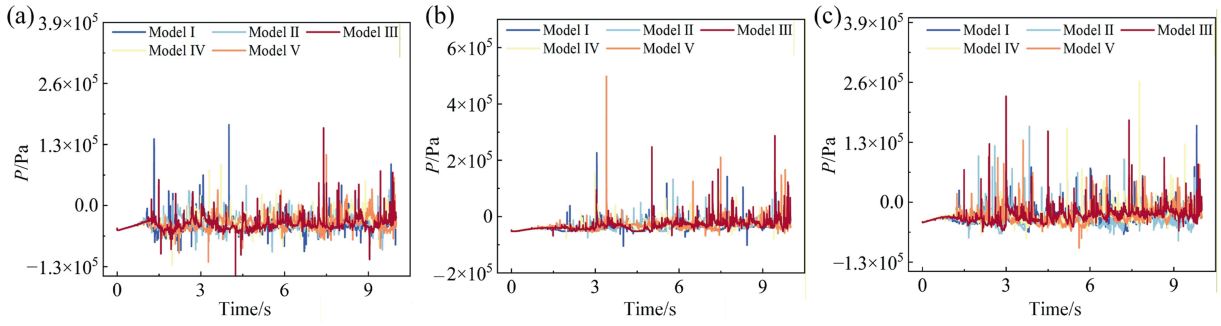


Fig. 5. Pressure pulsation distribution across various positions: (a) P1, (b) P4, and (c) P5.

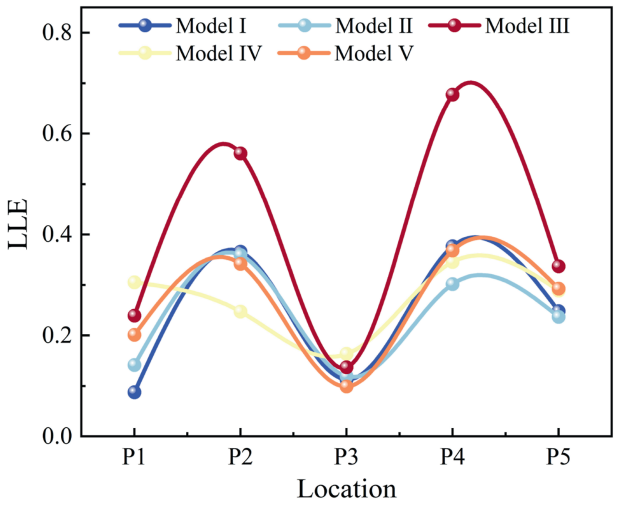


Fig. 6. LLE values under different models and positions.

models, indicating a strong chaotic characteristic. The LLE for model V is relatively high; this validates the potential of the asymmetric nozzle structure to excite chaotic behavior. The enhancement of chaotic performance means that nonlinear interactions between fluid microstructures in the molten bath are intensified, which in turn promotes the rapid diffusion and mixing of different phases within the melt. From a dynamic perspective, a larger LLE characterizes a faster exponential divergence of fluid trajectories within the phase space of the system. This implies more irregular relative motions between fluid particles and a substantially increased path separation rate. This characteristic is beneficial for enhancing the interaction between structures of different scales in the flow field; this promotes rapid exchange of matter and momentum over a larger spatial range and thus enhances macroscopic mixing performance. Overall, model III performs the best owing to the sustained dynamic disturbances introduced by its small-angle asymmetric structure. This structure facilitates bubble coalescence and vortex generation, which effectively increases the randomness and chaotic intensity of the flow field. By concentrating energy on the improvement of turbulent mixing efficiency, it avoids the energy dissipation caused by ineffective splashing, as observed in model I.

In summary, model III demonstrates considerable advantages in mixing efficiency and energy distribution owing to its asymmetric flow field design and optimized chaotic characteristics. However, although current studies have confirmed its marked advantages from the perspective of mixing and chaos, the spatiotemporal evolution mechanism of this model in energy transfer paths remains a subject worthy of further exploration.

4.3. Synchrosqueezed wavelet transforms

In bottom-blowing smelting, the SWT of pressure fluctuation signals is used to reveal differences in flow field dynamics across various models by analyzing their time–frequency characteristics. Fig. 7 presents the SWT results of the pressure fluctuation signals at the slag–metal interface wall position (P4) for all five models. The red arrows in Fig. 7 indicate the main energy concentration regions in the time–frequency domain, which are the high-energy intervals that appear as bright colors (white or light colors) in the synchronous continuous wavelet transform results. These regions correspond to the more active frequency components and notable multiscale dynamic responses in the flow field.

The frequency domain energy distribution shown in Fig. 7 highlights considerable differences in turbulent structures and energy transfer efficiency among the models. For models I and II, the energy is predominantly concentrated in the low-frequency range (50–150 Hz). While model II exhibits slightly higher frequency components and energy intensity than model I, both are dominated by large-scale vortices and lack an effective energy cascade process. Thus, turbulence development is insufficient and mixing performance is limited. In particular, model III exhibits a highly unique time–frequency characteristic. Its energy distribution spans a much broader range (50–300 Hz), and there are sharp fluctuations across different frequency bands. This indicates the presence of both robust large-scale vortices and active small-scale structures in the flow field. This characteristic clearly demonstrates that energy is efficiently transferred from large- to small-scale vortices *via* nonlinear interactions, forming a multiscale vortex cooperation that markedly strengthens mixing. Notably, model IV, while showing a similar spectral distribution pattern to that of model III, exhibits markedly lower energy amplitude in the key low-frequency range (50–150 Hz). This suggests that the intensity of large-scale vortex disturbances is insufficient, which limits the initiation of the energy cascade process. Model V, although exhibits a rich frequency spectrum, remains weak in the high-frequency range (250–300 Hz), indicating that small-scale vortices fail to properly receive energy, resulting in a disrupted energy cascade path.

In conclusion, model III, with its small-angle asymmetric nozzle design, successfully establishes an effective energy transfer path across multiple scales. This design highly enhances energy cascading effects, markedly improving turbulence excitation and mixing efficiency. Although the full-frequency energy distribution shows multiscale vortex cooperation, its spatial characteristics need to be further explored using POD mode decomposition.

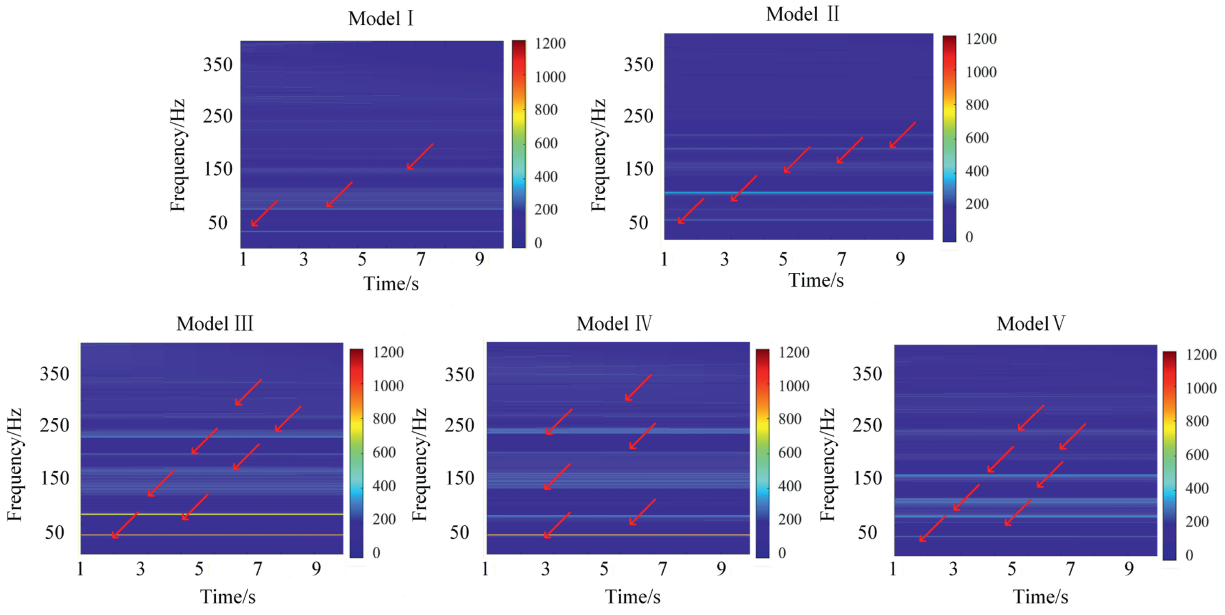


Fig. 7. Synchrosqueezed wavelet transform results at position P4 for different nozzle models.

4.4. POD energy distribution analysis

Herein, POD is used to analyze the velocity field to quantify the energy contribution of turbulent structures at different scales to the mixing process and identify the dominant modes. Fig. 8 presents the cumulative distribution of the energy contribution of the first 20 POD modes.

The analysis shows that model III excels in energy convergence efficiency, with the requirement of only 68 modes for reconstructing 98% of the total energy of the system. This number is notably lower than required by other models (model I requires 78 modes, model II requires 80 modes, and both models IV and V require 81 modes). Notably, the first two POD modes of model III together account for 71.36% of the total system energy. Alternatively, the corresponding values for the other models are as follows: model I: 38.65%, model II: 46.29%, model IV: 41.12%, and model V: 40.09%. The high concentration of energy in the lower modes gives model III a marked advantage in practical applications. This concentration of energy in the low-order modes suggests that model III has better potential for model simplification, meaning its flow characteristics can be accurately represented by only a few dominant modes. This provides strong support for real-time flow control and fast numerical simulations.

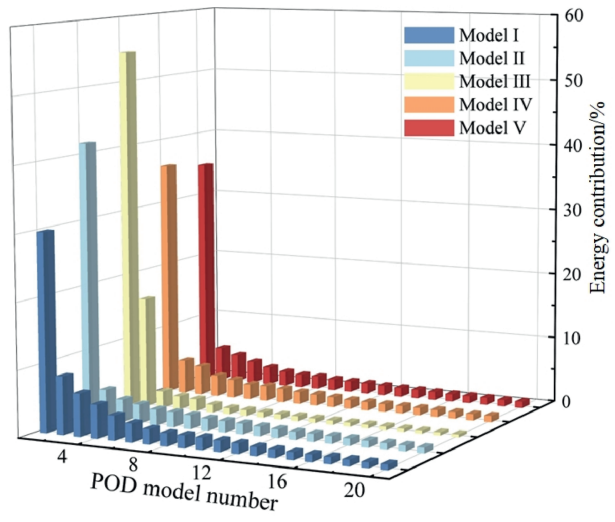


Fig. 8. Energy contributions of the first 20 POD modes postprocessing.

Furthermore, this notable difference indicates that the flow field structure of model III contains a highly organized large-scale circulation core that can effectively organize and transfer energy. Notably, the energy concentration in the low-order modes complements the results from the continuous wavelet transform analysis. While the POD analysis reveals a powerful energy organization and transport core in the flow field, the wavelet analysis shows that this core structure can efficiently excite multiscale turbulence and promote energy cascade. The combination of these two characteristics constitutes the fundamental reason for the marked advantage of model III in improving mixing efficiency. It has both a strong energy driving source and an efficient energy transfer path, achieving the best balance between “ordered driving” and “disordered mixing,” which is difficult to achieve in other models. The flow field structure characteristics of model III shall be further analyzed using POD streamlines in subsequent studies.

4.5. POD streamline plot

On the basis of the clarified energy distribution characteristics, the physical causes are further revealed through the instantaneous flow field structure. Using the instantaneous velocity streamlines at 2 s (Fig. 9), this work compares and analyzes the velocity distribution and flow field structure features of different models.

Specifically, models I and III show similar distribution trends. The high-speed regions are primarily concentrated in the mixing area at the center of the flow field, while the streamlines near the wall are relatively sparse, and the velocity values are lower. In particular, the overall velocity in model III is considerably higher than that in model I. However, models II, IV, and V exhibit distinctly different characteristics. Although their overall velocities are comparable to those of model III, dense streamlines and

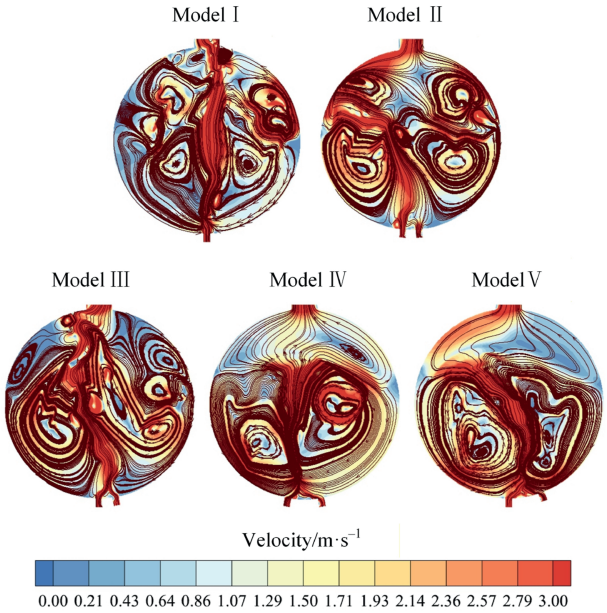


Fig. 9. Velocity streamline plots of different models at t= 2 s.

localized high-speed regions appear near the wall. This type of flow field structure is especially unfavorable in the flow–slag mixing system. It suggests strong shear effects on the wall, which can exacerbate equipment wear and affect long-term operational life. The flow field structure of model III is considerably superior. Its streamline pattern is the most complex and filled with multiscale, high-intensity vortex structures. The complex flow field structure highly facilitates the mixing of fluid microstructures and momentum exchange, making it an ideal flow field to achieve efficient mixing. *Via* comprehensively analyzing these flow field features, model III, with its high-speed flow concentrated in the mixing zone, effective protection of the wall, and excellent multiscale vortex structures, is confirmed to exhibit the best mixing potential.

POD is performed on the original velocity field to deeply analyze the dynamic mechanisms of multiscale vortex structures in the instantaneous flow field. The POD analysis clearly reveals the essential differences between the models in terms of their dominant flow structures and energy transfer processes. On the basis of the preceding energy spectrum analysis, the selected number of modes in this work sufficiently captures the main energy contributions of the flow field and ensures the comparability of the POD results among different models, thereby meeting the requirements for the subsequent multiscale flow structure analysis.

Fig. 10(a) illustrates the streamline distribution of the 1st mode for each model. This mode represents the dominant structure in the flow field, which accounts for the highest proportion of energy and is the most stable. It can be observed that models I, II, IV, and V display a regular, symmetric double-vortex structure, indicating that their flow fields are controlled by a pair of dominant vortices with similar scales and intensities. Conversely, the 1st mode of model III undergoes a fundamental change; its symmetry breaks and evolves into an asymmetric large-scale vortex that occupies a dominant position, and its structure covers the molten pool area more comprehensively. Notably, this asymmetry helps drive the fluid to move over a larger area, effectively avoiding the common “dead zones” observed in symmetric flow fields, thereby laying a solid foundation for achieving global efficient mixing. Although in the 2nd mode (Fig. 10(b)), the vortex size of model III is relatively large compared with that of the other models, the 1st mode already dominates most of the energy and basic shape of the flow field, establishing the advantages of model III in vortex structure distribution. Further observation of the higher-order modes (3rd and 4th modes, Fig. 10(c) and (d)) reveals that all models begin to develop dense intermediate and small-scale vortex structures at the edges of large vortices and shear layers. This phenomenon is particularly pronounced in model III. This feature corroborates the results from the continuous wavelet transform analysis, showing that the dominant large vortices in model III can continuously excite and nurture such small-scale vortex structures *via* an efficient energy cascading process. This “large vortex-driven, small vortex dissipation” multiscale collaborative mechanism markedly enhances the mixing efficiency of fluid microstructures and momentum exchange, leading to a much higher energy utilization rate than that of other models. By the 11th mode (Fig. 10(e)), the difference becomes even more apparent. The flow field of asymmetric models (models III and V) contains abundant intermediate and small-scale vortex structures, with dense streamlines, indicating that considerable energy remains at this scale. Conversely, the flow field of symmetric models (models II and IV) shows sparse vortex structures, signaling that energy in this mode has almost dissipated. This demonstrates that asymmetric models maintain more active turbulent fluctuations and stronger energy transfer capabilities across the entire energy spectrum.

In summary, combining the previous observations of instantaneous velocity streamlines, the POD analysis confirms at the dynamic mechanism level that model III, with its small-angle asymmetric structure and the unique multiscale vortex synergistic effect it generates, is comprehensively advantageous in improving mixing performance. Its flow field not only breaks through the spatial limitations of the mixing range through asymmetric large vortices but also notably enhances the conversion and dissipation efficiency of kinetic energy using continuously active intermediate and small-scale vortex structures.

4.6. POD mode temporal coefficient analysis

Upon analyzing the spatial structure of the POD modes, an examination of their time coefficients reveals the dynamic evolution behavior and stability of the flow structures represented by each mode. The aperiodic evolution of the POD time coefficients represents chaotic flow at the modal level, and its modulation characteristics reflect the energy exchange process between flow structures of different scales. Fig. 11 presents the time coefficient curves for the 2nd–5th POD modes of the five models (the 1st mode is not shown towing to its dominant position and weak time-varying characteristics).

The analysis that the high-order time coefficients of all models nonperiodically fluctuate, which confirms the presence of turbulences in the flow field. However, marked differences exist among the models in terms of energy accumulation time, *i.e.*, the duration during which the time coefficient remains in a steady oscillation phase (highlighted using the green box in Fig. 11). Specifically, models I and III have the longest accumulation time, followed by that of models II and IV, with model V having the shortest. This difference is of high physical importance, as the duration of energy storage directly correlates with the dynamic stability of the system. Model III shows a long duration of steady oscillation, indicating that the accumulation and release of energy in its flow field reach a dynamic equilibrium. Conversely, the

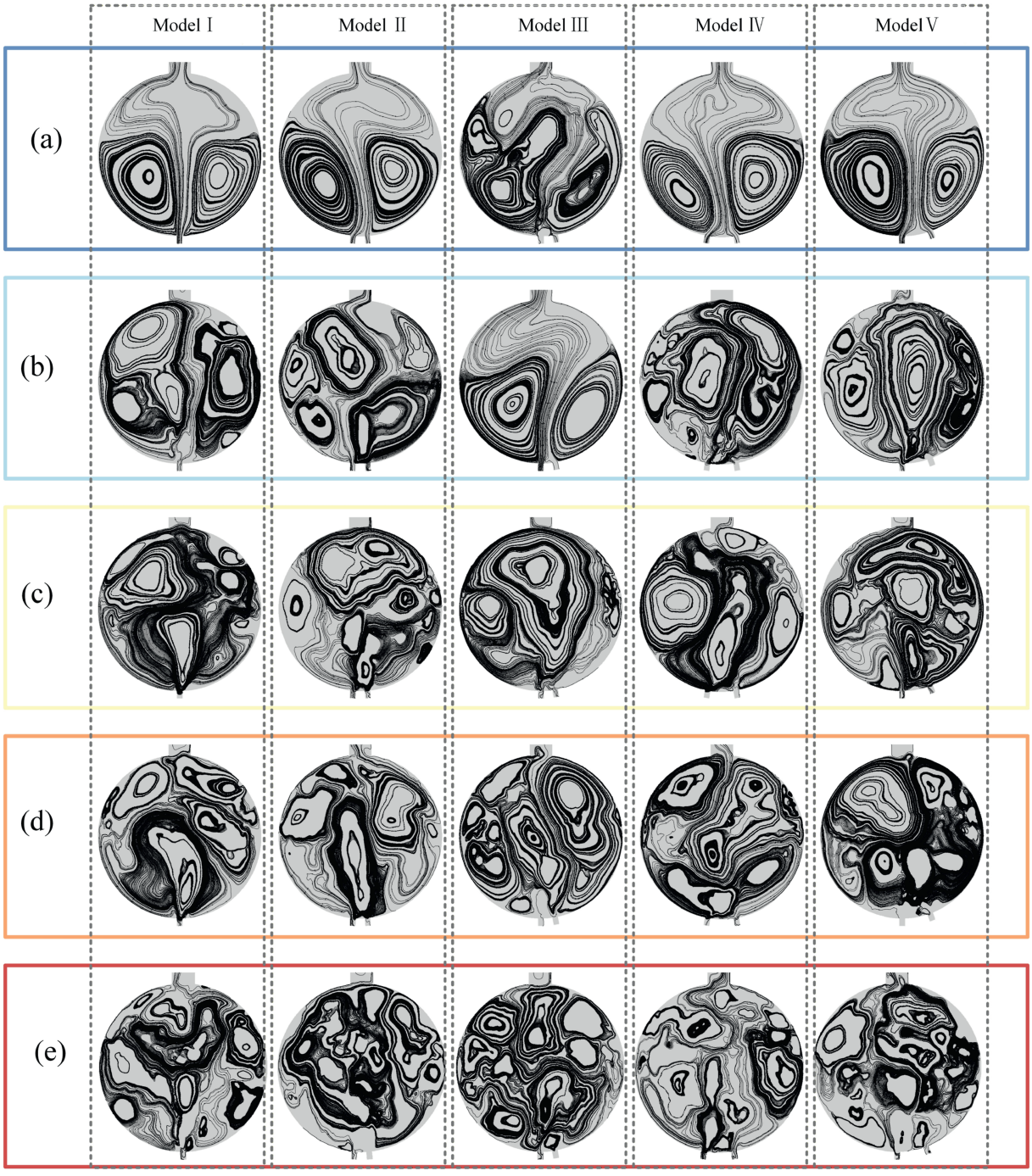


Fig. 10. Streamlines of the POD modes: (a) 1st mode, (b) 2nd mode, (c) 3rd mode, (d) 4th mode, and (e) 11th mode.

shorter accumulation time in model V implies that its flow structure is more prone to instability and can frequently trigger intermittent strong turbulence. Upon further observation, the time coefficient curve of model III (Fig. 11(c)) exhibits a particularly unique shape. Its fluctuation amplitude is the most gradual, with no sharp jumps. This feature highly suggests that its energy transfer process is governed by a dynamic balancing mechanism, which is modulated by chaotic nonlinear effects. This stability is not a result of rapid energy dissipation; rather, it results from multiscale coupling. The nonlinear interactions between high- and low-frequency fluctuations facilitate the uniform redistribution of energy across different-scale vortex structures. This mechanism effectively prevents energy from accumulating locally to form singularities, such as sudden velocity gradient changes, thereby suppressing the generation of sudden turbulence.

The dynamic characteristics, including persistent energy storage and smooth chaotic modulation, lead to a clear conclusion: the flow field of model III exhibits stronger chaotic characteristics. This generally corresponds to a larger LLE, which quantitatively explains its exceptional mixing ability and inherent stability from a dynamic perspective.

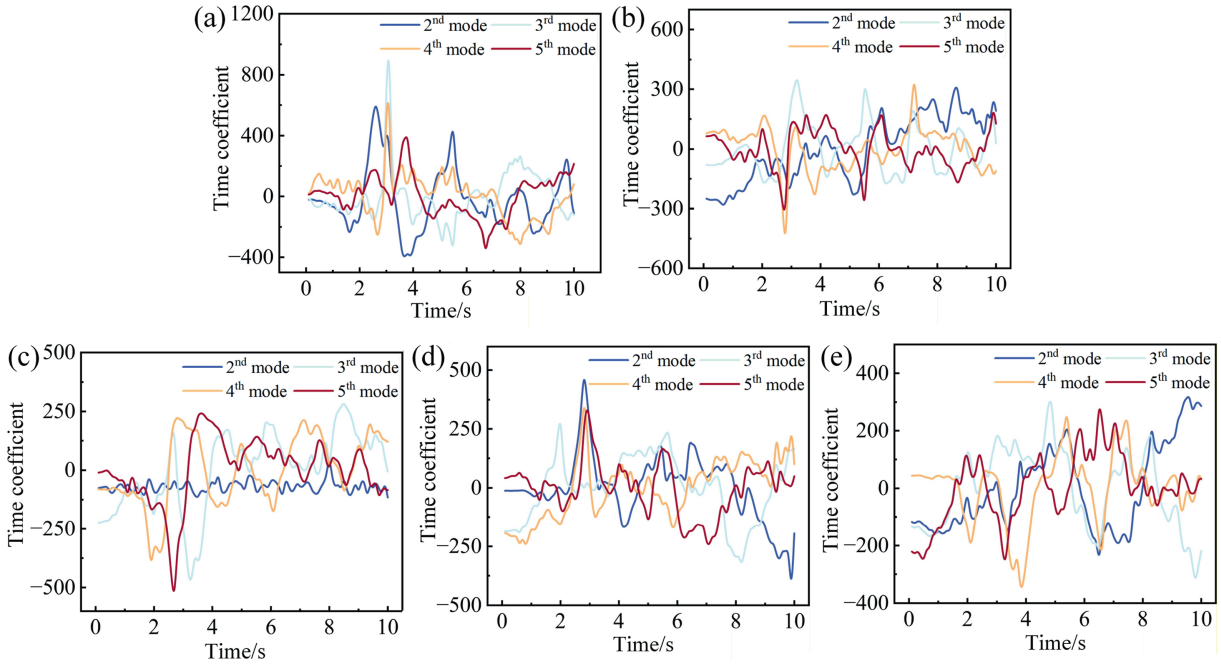


Fig. 11. Analysis of temporal coefficient distributions for POD modes 2nd–5th in different models: (a) model I, (b) model II, (c) model III, (d) model IV, and (e) model V.

5. Conclusions

A combination of chaos theory with POD techniques was employed to analyze and compare the five furnace models under the same airflow rate. The multiscale flow characteristics of the bottom-blown molten pools were analyzed on the basis of the following two complementary perspectives: temporal dynamics and spatial structure. The five furnace models were analyzed and compared under the same gas flow rate to confirm the superior performance of the furnace with a small-angle asymmetric nozzle arrangement in enhancing chaotic mixing and energy cascading. The conclusions derived are as follows.

1. In terms of bubble dynamics and macroscopic flow field structure, different nozzle arrangements markedly altered bubble generation, rising, and merging behaviors and thereby modulated the main circulation morphology of the molten pool. Compared with symmetrical configurations, asymmetrical nozzles were more conducive to forming a circulation structure with a wider coverage and stronger disturbance persistence; this enhanced the melt convection and energy utilization without relying on violent splashing.
2. From a time–dynamics perspective, the LLE calculated on the basis of pressure pulsation signals indicated marked differences in chaos intensity among different models. Higher LLE values correspond to faster phase–space trajectory divergence rates, reflecting stronger nonlinear interactions and instabilities in the flow field. This enhanced chaotic characteristic provides favorable dynamic conditions for the frequent reorganization of fluid particles and phase diffusion.
3. Time–frequency analysis revealed the characteristics of cross-scale energy transfer. SWT showed that the model with strong chaotic characteristics maintained a high energy level over a wider frequency band, indicating that the continuous energy transfer process was strengthened from large- to small-scale vortex structures, and the energy cascade effect was substantially enhanced; this effectively excited turbulence and enhanced mixing.
4. POD analysis supplemented the above dynamic understanding from the perspective of spatial structure. The dominant mode revealed the asymmetric large-scale vortex structure formed under the asymmetric nozzle configuration, while the persistent small- and medium-scale vortices in the higher-order modes indicated that the flow field possessed additional active multiscale cooperative characteristics. This spatial organization of the vortex structure provided a structural basis for cross-scale energy cascading.

In summary, the POD method and chaos analysis characterized the same physical process from different dimensions. The former quantitatively described the nonlinearity and chaos intensity of the flow, while the latter revealed the spatial distribution and energy organization of multiscale vortex structures. Their corroboration demonstrated that the asymmetric nozzle configuration reached a more efficient and stable mixing state by enhancing turbulent chaos and multiscale energy transfer paths. From an engineering application perspective, this analytical framework provided a quantifiable and comparable evaluation method for the design and optimization of bottom-blown furnace nozzle structures and operating parameters. This enabled systemic decision-making on the basis of flow dynamics and energy transfer mechanisms, rather than solely relying on experience or single mixing indices, thus providing theoretical support for achieving efficient, stable, and low-loss smelting processes.

CRediT Authorship Contribution Statement

Yu Wang: Writing – original draft, Software, Investigation, Data curation. Tong Meng: Validation, Investigation, Data curation. Shuang Qin: Software, Data curation. Guocan Zheng: Writing – review & editing. Jun Du: Writing – review & editing, Supervision. Shibo Wang: Project administration. Changyuan Tao:

Methodology, Formal analysis. Zuohua Liu: Writing – review & editing, Supervision, Conceptualization.

Data Availability

The original data that support the findings of this work are available on request from the corresponding author.

Declaration of Competing Interest

The authors declare that they have no known competing financial interests or personal relationships that could have appeared to influence the work reported in this paper.

Acknowledgements

This work was supported by Open Fund of State Key Laboratory of Complex Nonferrous Metal Resources Clean Utilization (CNMRCUKF2406), Chongqing Natural Science Foundation Innovation and Development Joint Fund Project (CSTB2022NSCQ-LZX0014), and Fundamental Research Funds for Central Universities (2022CDJQY-005). At the same time, this work also received funding from the China Scholarship Council and Young Elite Scientists Sponsorship Program for Doctoral Students by the China Association for Science and Technology (CAST) to Tong Meng.

References

[1] S.S. Wang, X. Xiong, P.Q. Liu, Q.Z. Zhang, Q. Zhang, C.Y. Tao, Y.D. Wang, Z.H. Liu, CFD simulation of hydrodynamics and mixing performance in dual shaft eccentric mixers, *Chin. J. Chem. Eng.* 62 (2023) 297–309.
[2] J.K. Sun, J.S. Zhang, W.H. Lin, X.M. Feng, Q. Liu, Effect of bottom blowing mode on fluid flow and mixing behavior in converter, *Metals* 12 (1) (2022) 117.
[3] K.Z. Song, A. Jokilaakso, Transport phenomena in copper bath smelting and converting processes—a review of experimental and modeling studies, *Miner. Process. Extr. Metall. Rev.* 43 (1) (2022) 107–121.
[4] L. Zhang, K. Yang, M. Li, Q.T. Xiao, H. Wang, Chaotic characterization of macromixing effect in a gas–liquid stirring system using modified 0–1 test, *Can. J. Chem. Eng.* 100 (2) (2022) 261–275.
[5] S. Xie, C.F. Liao, B.J. Zhao, Kinetic and thermodynamic studies on lead-rich slag reduction at various CaO/SiO_2 ratios, *JOM* 74 (9) (2022) 3625–3633.
[6] W. Wang, L.Z. Mu, H.L. Zhao, X.Y. Cai, F.Q. Liu, H.Y. Sohn, CFD study on improvement of non-uniform stirring in a large bottom-blown copper smelting furnace, *Min. Metall. Explor.* 41 (3) (2024) 1421–1435.
[7] T.T. Lu, L.Z. Mu, Y.D. Xiao, H.L. Zhao, F.Q. Liu, CFD study on bottom-blown copper smelting furnace with unsymmetric gas injection, *J. Sustain. Metall.* 8 (3) (2022) 1235–1244.
[8] S. Ganguly, S. Chakraborty, Numerical modelling studies of flow and mixing phenomena in gas stirred steel ladles, *Ironmak. Steelmak.* 35 (7) (2008) 524–530.
[9] K.Z. Song, A. Jokilaakso, CFD modeling of multiphase flow in an SKS furnace with new tuyere arrangements, *Metall. Mater. Trans. B* 53 (1) (2022) 253–272.
[10] H. Hu, L.Z. Yang, Y.F. Guo, F. Chen, S. Wang, F.Q. Zheng, B. Li, Numerical simulation of bottom-blowing stirring in different smelting stages of electric arc furnace steelmaking, *Metals* 11 (5) (2021) 799.
[11] P. Shao, L.P. Jiang, Flow and mixing behavior in a new bottom blown copper smelting furnace, *Int. J. Mol. Sci.* 20 (22) (2019) 5757.
[12] L. Shui, Z.X. Cui, X.D. Ma, M.A. Rhamdhani, A. Nguyen, B.J. Zhao, Mixing phenomena in a bottom blown copper smelter: A water model study, *Metall. Mater. Trans. B* 46 (3) (2015) 1218–1225.
[13] B.C. Jiang, X.Y. Guo, Q.M. Wang, Analysis of melt flow characteristics in large bottom-blowing furnace strengthened by oxygen lance jet at different positions, *J. Sustain. Metall.* 9 (4) (2023) 1704–1715.
[14] L. Shui, Z.X. Cui, X.D. Ma, M.A. Rhamdhani, A.V. Nguyen, B.J. Zhao, Understanding of bath surface wave in bottom blown copper smelting furnace, *Metall. Mater. Trans. B* 47 (1) (2016) 135–144.
[15] J.L. Liow, N.B. Gray, Slopping resulting from gas injection in a Peirce–Smith converter: Water modeling, *Metall. Trans. B* 21 (6) (1990) 987–996.
[16] X.B. Zhou, M. Ersson, L.C. Zhong, P.G. Jönsson, Numerical and physical simulations of a combined top-bottom-side blown converter, *Steel Res. Int.* 86 (11) (2015) 1328–1338.
[17] O. Olivares, A. Elias, R. Sánchez, M. Díaz-Cruz, R.D. Morales, Physical and mathematical models of gas–liquid fluid dynamics in LD converters, *Steel Res.* 73 (2) (2002) 44–51.
[18] S. Sarkar, N. Sen, K.K. Singh, Bubble formation at top-submerged nozzles immersed in a quiescent liquid, *Prog. Nucl. Energy* 161 (2023) 104709.
[19] D.X. Wang, Y. Liu, Z.M. Zhang, P. Shao, T.A. Zhang, Experimental study of bottom blown oxygen copper smelting process for water model, *AIP Conf. Proc.* 1542 (1) (2013) 1304–1307.
[20] H.L. Zhao, J.Q. Wang, F.Q. Liu, H.Y. Sohn, Flow zone distribution and mixing time in a Peirce: Smith copper converter, *Int. J. Miner. Metall. Mater.* 29 (1) (2022) 70–77.
[21] M.M. Li, L. Li, Q. Li, Z.S. Zou, Modeling of mixing behavior in a combined blowing steelmaking converter with a filter-based Euler–Lagrange model, *JOM* 70 (10) (2018) 2051–2058.
[22] Z.Y. Du, S.L. Yang, G.R. Bao, H. Wang, Numerical study of swirling effect on enhancing the bath dynamics in the top-submerged-lance furnace, *Metall. Mater. Trans. B* 54 (6) (2023) 3115–3129.
[23] S.C. Du, Modeling related to secondary steel making, *Steel Res. Int.* 83 (9) (2012) 825–841.
[24] Z.S. Yang, L.Z. Yang, T. Cheng, F. Chen, F.Q. Zheng, S. Wang, Y.F. Guo, Fluid flow characteristic of EAF molten steel with different bottom-blowing gas flow rate distributions, *ISIJ Int.* 60 (9) (2020) 1957–1967.
[25] X. Liu, A.J. Xu, F. Yuan, C.B. Pang, Optimisation of the bottom blowing process for a 200 t converter, *Ironmak. Steelmak.* 50 (1) (2023) 1–12.
[26] Z.Y. Lai, Z. Xie, L.C. Zhong, Influence of bottom tuyere configuration on bath stirring in a top and bottom combined blown converter, *ISIJ Int.* 48 (6) (2008) 793–798.
[27] Q. Guo, C.M. Boyce, Structured bubbling in layered gas-fluidized beds subject to vibration: A CFD-DEM study, *AIChE J.* 68 (7) (2022) e17709.
[28] Q. Guo, Y.X. Zhang, A. Padash, K.N. Xi, T.M. Kovar, C.M. Boyce, Dynamically structured bubbling in vibrated gas-fluidized granular materials, *Proc Natl Acad Sci USA.* 118 (35) (2021) e2108647118.
[29] Q. Guo, S. Chiu, W. Da, C.M. Boyce, Heat transfer within dynamically structured bubbling fluidized beds subject to vibration: A two-fluid modeling study, *AIChE J.* 69 (2) (2023) e17970.
[30] B. Begiashvili, N. Groun, J. Garicano-Mena, S. Le Clainche, E. Valero, Data-driven modal decomposition methods as feature detection techniques for flow problems: A critical assessment, *Phys. Fluids* 35 (4) (2023) 041301.
[31] R. Raju, S. Balachandar, D.F. Hill, R.J. Adrian, Reynolds number scaling of flow in a stirred tank with Rushton turbine. Part II: Eigen decomposition of fluctuation, *Chem. Eng. Sci.* 60 (12) (2005) 3185–3198.
[32] F. Mendoza, A.L. Bañales, E. Cid, C. Xuereb, M. Poux, D.F. Fletcher, J. Aubin, Hydrodynamics in a stirred tank in the transitional flow regime, *Chem. Eng. Res. Des.* 132 (2018) 865–880.
[33] A. de Lamotte, A. Delafosse, S. Calvo, D. Toye, Analysis of PIV measurements using modal decomposition techniques, POD and DMD, to study flow structures and their dynamics within a stirred-tank reactor, *Chem. Eng. Sci.* 178 (2018) 348–366.
[34] A. de Lamotte, A. Delafosse, S. Calvo, D. Toye, Identifying dominant spatial and time characteristics of flow dynamics within free-surface baffled stirred-tanks from CFD simulations, *Chem. Eng. Sci.* 192 (2018) 128–142.
[35] A. Liné, J.C. Gabelle, J. Morchain, D. Anne-Archard, F. Augier, On POD analysis of PIV measurements applied to mixing in a stirred vessel with a shear thinning fluid, *Chem. Eng. Res. Des.* 91 (11) (2013) 2073–2083.
[36] T. Meng, Y. Wang, S. Qin, P.Q. Liu, Y.D. Wang, C.Y. Tao, Z.H. Liu, Complex flow field analysis in multi-shaft stirred reactors: Dynamics of wave-vortex coupling revealed by POD and DMD methods, *Chem. Eng. Sci.* 301 (2025) 120753.
[37] T. Meng, A. Paglianti, F. Alberini, G. Montante, Y. Wang, Z.H. Liu, Investigating coupling and intensification mechanisms in multi-shaft digesting stirring reactors using POD, *AIChE J.* 71 (11) (2025) e70028.
[38] T. Meng, Y. Wang, S.S. Wang, S. Qin, Q. Zhang, Y.D. Wang, C.Y. Tao, Y.Q. Xu, Z. H. Liu, Exploration of multishafts stirred reactors: An investigation on experiments and large eddy simulations for turbulent chaos and mixing characteristics, *Ind. Eng. Chem. Res.* 63 (5) (2024) 2441–2456.
[39] T. Meng, J. Yang, S.S. Wang, Y. Wang, S. Qin, Y.D. Wang, C.Y. Tao, Q. Zhang, Z. H. Liu, Multi-shaft stirred reactors mixing efficiency: Rapid characterization strategy based on chaotic attractors, *AIChE J.* 70 (10) (2024) e18510.
[40] T. Meng, Y. Wang, S. Qin, P.Q. Liu, Q. Zhang, Y.D. Wang, C.Y. Tao, Z.H. Liu, From patterns to cocktails: A novel visualization method for turbulent flow fields in stirred reactors, *Ind. Eng. Chem. Res.* 63 (44) (2024) 19320–19328.
[41] S.L. Brunton, B.R. Noack, P. Koumoutsakos, Machine learning for fluid mechanics, *Annu. Rev. Fluid Mech.* 52 (2020) 477–508.
[42] H.F. Liu, Y.Z. Yang, Z.H. Dai, Z.H. Yu, The largest Lyapunov exponent of chaotic dynamical system in scale space and its application, *Chaos* 13 (3) (2003) 839–844.
[43] I. Daubechies, J.F. Lu, H.T. Wu, Synchrosqueezed wavelet transforms: An empirical mode decomposition-like tool, *Appl. Comput. Harmon. Anal.* 30 (2) (2011) 243–261.
[44] J. Lumley, Stochastic Tools in Turbulence, Academic Press, New York and London, 2007.

[45] L. Sirovich, Turbulence and the dynamics of coherent structures. I. Coherent structures, *Q. Appl. Math.* 45 (3) (1987) 561–571.
[46] K. Fukunaga, Introduction to Statistical Pattern Recognition, 2nd, Elsevier, Amsterdam, 1990.
[47] Y.N. Wang, L.L. Cao, Z.F. Cheng, B. Blanpain, M.X. Guo, Mathematical methodology and metallurgical application of turbulence modelling: A review, *Metals* 11 (8) (2021) 1297.
[48] ANSYS, ANSYS Fluent Theory Guide 19.1, ANSYS, Canonsburg, PA, 2019.
[49] M.A. Ramírez-Argáez, Numerical simulation of fluid flow and mixing in gas-stirred ladles, *Mater. Manuf. Process.* 23 (1) (2007) 59–68.
[50] Y. Liu, M. Ersson, H.P. Liu, P.G. Jönsson, Y. Gan, A review of physical and numerical approaches for the study of gas stirring in ladle metallurgy, *Metall. Mater. Trans. B* 50 (1) (2019) 555–577.
[51] B.C. Jiang, X.Y. Guo, Q.M. Wang, Two-dimensional analysis of melt pneumatic stirring in large bottom blowing furnace based on CFD, *Nonferrous Met. Extr. Metall. (6) (2023) 39–50.*
[52] H.J. Yan, F.K. Liu, Z.Y. Zhang, Q. Gao, L. Liu, Z.X. Cui, D.B. Shen, Influence of lance arrangement on bottom-blowing bath smelting process, *Chin. J. Nonferrous Metals* 22 (8) (2012) 2393–2400.